Knee Exoskeleton-Enabled Balance Control of Human Walking Gait With Unexpected Foot Slip

Chunchu Zhu , Graduate Student Member, IEEE, and Jingang Yi , Senior Member, IEEE

Abstract—Foot slip is one of the leading causes of fall-related injuries during human walking. The underlying slip dynamics help understand bipedal recoverability under gait perturbation and therefore provide a tool to design proactive slip-induced fall prevention strategies. We present a new integrated wearable sensing and exoskeleton-enabled fall prevention under unexpected foot slip. The real-time slip detection is realized with a set of small, wearable inertial measurements units on both legs. We use the balance recoverability and inter-limb coordination analyses to design the balance recovery strategies. The bilateral knee exoskeleton provides assistive torque control and helps walker to follow the designed gait recovery strategies. Multiple subject experiments are presented to demonstrate the exoskeleton-enabled recovery under foot slip. Various critical metrics, including slip distance, velocity, swing leg touch-down time, are systematically compared to assess the efficacy of both the exoskeleton and the controller. The results confirm that incorporating knee exoskeletons as a balance recovery method for human walking is a reliable and robust approach to mitigate or prevent slip-induced falls.

Index Terms—Bipedal walking, foot slip, balance control, exoskeleton control, slip mechanics.

I. INTRODUCTION

ALLS in elderly and occupational population present major health risks and fall-induced injuries is the second largest contributor for economic burden in the US [1]. It is imperative to design effective fall prevention intervention to mitigate and reduce the slip-induced fall injuries. Wearable robots such as exoskeletons provide assistive balance torques that would help walkers towards successful slip recovery and prevent slip-induced falls. Compared with normal walking gaits, the knee joints have higher torque variations during unexpected foot slip [2]. In [3], large knee torque peak and its rate values are suggested for slip balance recovery. Therefore, it is desirable to develop a knee exoskeleton-enhanced balance control

Manuscript received 12 May 2023; accepted 15 September 2023. Date of publication 4 October 2023; date of current version 16 October 2023. This letter was recommended for publication by Associate Editor D. Novak and Editor J.-H. Ryu upon evaluation of the reviewers' comments. This work was supported by the US National Science Foundation under Grants CMMI-1762556 and CNS-1932370. (Corresponding author: Jingang Yi.)

This work involved human subjects or animals in its research. Approval of all ethical and experimental procedures and protocols was granted by Institutional Review Board (IRB) at Rutgers University under Application No. Pro2019001607.

The authors are with the Department of Mechanical and Aerospace Engineering, Rutgers University, Piscataway, NJ 08854 USA (e-mail: chunchu.zhu@rutgers.edu; jgyi@rutgers.edu).

This letter has supplementary downloadable material available at https://doi.org/10.1109/LRA.2023.3322082, provided by the authors.

Digital Object Identifier 10.1109/LRA.2023.3322082

of walking gait under unexpected slip perturbation. Most control designs of wearable exoskeleton focus on human walking, running, kneeling, and other steady gaits for rehabilitation and assistive tasks [4], [5], [6], [7], [8]. All of the above-mentioned control however cannot be applied directly to balance recovery under foot slip because the slip and transient gait dynamics are rapidly changing, particularly for unexpected slip. New recovery analysis and control design are needed for slip-induced biped dynamics.

Simple linear inverted pendulum (LIP) model or its variations capture the basic bipedal walking locomotion properties. The simplicity of LIP models is attractive for analyzing relationship between center of mass (COM), zero moment point (ZMP) and motion stability. In [9], capture point (CP) was utilized to describe human balance and to inspire the design of control systems for humanoid robots. The work in [10] extended the CP concept and proposed a balance recoverability region that was used to design balance controller for a bipedal robot under foot slip [11], [12]. The work in [13], [14] used hybrid zero dynamic (HZD) models to design stable gaits under foot slip and a feedback control was considered to stabilize the gait. The above controllers were mainly for bipedal robots and are not directly applicable for human walkers under unexpected foot slip due to complex human-robot interactions. Although the HZD control approach was extended to control lower-limb powered exoskeletons in [15], it mainly dealt with steady walking gaits.

A few recent studies discussed human balance recovery analysis under foot slip. An attempt was made in [16] to develop a wearable knee assistive device to potentially prevent slip-induced falls but no human slip recovery experiments were conducted. The study in [17] demonstrated the use of a hip exoskeleton in assisting elderly and disabled individuals with balance recovery during unexpected slips. However, the work did not present a systematic analysis or design of the exoskeleton controller. The joint angle-based slip detection, although sufficient to prevent false positives, took longer time than human neural controller. Moreover, the study in [17] used slip-like perturbations on a treadmill, which did not accurately capture a real-life foot slip scenario where the slipping leg moves relative to the ground and causes unpredictable motion dynamics.

In this letter, we present a new integrated wearable sensing and exoskeleton-enabled balance recovery control of human walking under unexpected foot slip. The bilateral exoskeleton controller, inspired by human neural control, leverages coordinated motion between the slipping stance and the swing legs. We achieve real-time slip detection through seven wearable inertial measurement

2377-3766 © 2023 IEEE. Personal use is permitted, but republication/redistribution requires IEEE permission. See https://www.ieee.org/publications/rights/index.html for more information.

units (IMUs) attached to the lower limbs. Compared to [18], the slipping velocity estimation in this work is implemented in real time. Furthermore, we extend the two-mass LIP (TMLIP) model and consider the foot base of support, rather than the foot point contact, as those in [10], [13], [14]. The extended recoverability analysis includes the actuation bounds and therefore, generates the feasible targeted recovery motion profile. We also present a multi-level exoskeleton controller design to use the quasi-direct drive prototype of a lightweight and flexible knee exoskeletons [6], [19]. Human subject experiments demonstrate the effectiveness of the balance recovery analysis and control. The main contribution of this work lies in the exoskeleton-enabled balance recovery control of human walkers under unexpected foot slip. Our work represents the first systematic design of knee exoskeleton-enabled slip recovery control.

The remainder of this letter is organized as follows. We present the slip dynamics and analysis in Section III. Section III discusses the slip recovery controller design. Section IV describes the experiments and Section IV-B presents the experimental results. Finally, we discuss the concluding summary in Section V.

II. SLIP DYNAMICS AND RECOVERABILITY

A. Two-Mass LIP Model With Foot Slip

Fig. 1 shows a set of snapshots of two types of slip-induced falls during human walking experiments. Fig. 1(a) shows the instability-induced fall at the heel touchdown, whereas Fig. 1(b) illustrates an example of limb-collapse-induced fall. Instabilityinduced fall happens when one foot (i.e., right foot) starts to slip after the heel touchdown and the left foot toeoff. The walker tries to land the swing leg to the ground and to recover from slip perturbation. Finally, the gait stability is lost after swing leg touchdown, as shown in Fig. 1(a). For limb-collapse-induced fall, the recovered gait is stable but the lower limbs cannot sustain the gait stability due to weak joint support [20], as shown in Fig. 1(b).

A TMLIP model is used to capture the human walking motion under foot slip. Fig. 2(a) illustrates the human lower-limb configuration for IMU-based real-time slip detection, while Fig. 2(b) shows the kinematic configuration for the TMLIP model for the single-stance phase. As explained in [10], [21], instead of using single point mass, the introduction of the TMLIP model mainly captures the additional degree-of-freedom (DOF) of the foot sliding motion and also allows that the center of pressure (COP) can be positioned independently with the stance foot.

As shown in Fig. 2(b), motions are assumed only in the sagittal plane and two masses, m_1 and m_2 , are connected by a massless rod. Mass m_1 represents the human body and m_2 for the stance leg. Same to most LIP models, the height of m_1 is denoted as z_c and is assumed constant. In inertial frame \mathcal{N} , the horizontal positions of m_1 and m_2 are denoted as x_1 , and x_s , respectively. The COP location is denoted as P and its horizontal position is denoted as u.

Defining $\delta = x_1 - x_s$ as the horizontal distance between m_1 and m_2 and $u_r = x_s - u$, the motion dynamics under normal walking without foot slip is [10]

$$\Sigma_{ns}: \ddot{\delta} = \omega_{ns}^2 \left(\delta + r_m u_r\right) \tag{1}$$

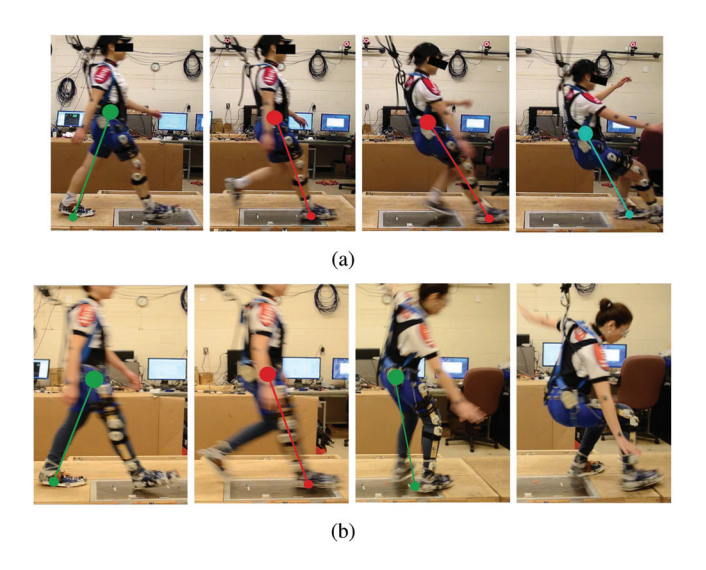


Fig. 1. Two types of slip-induced falls during human walking experiments. (a) Instability-induced fall at the instant of right foot touchdown and left foot toeoff. (b) Limb-collapse-induced fall.

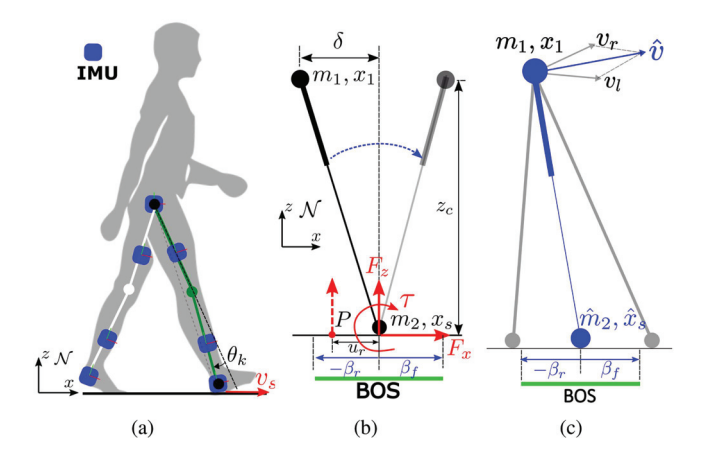


Fig. 2. (a) Schematic of a human lower-limb motion with multiple wearable IMUs for slip detection and estimation. (b) A schematic of the TMLIP model at single-stance phase. (c) Schematic of a treatment of the "virtual" TMLIP model during double-stance phase.

and under foot slip, the motion dynamics model becomes

$$\Sigma_s: \ddot{\delta} = \omega_s^2 \left(\delta + r_m u_r + \mu z_c \right), \tag{2}$$

 $\Sigma_s: \ddot{\delta} = \omega_s^2 \left(\delta + r_m u_r + \mu z_c \right), \tag{2}$ where $\omega_{ns} = \sqrt{\frac{g}{z_c}}$ and $\omega_s = \sqrt{\frac{r_m}{r_m - 1}} \omega_{ns}, r_m = \frac{m_1 + m_2}{m_1}, \mu$ is the foot/ground friction coefficient, and g is the gravitational constant. The main difference between models Σ_{ns} and Σ_{s} lies in frequency parameters ω_{ns} and ω_{s} and an additional constant term μz_c in (2).

To maintain balance, the COP must be within the base of support (BOS). Denoting the BOS boundaries (in the x-direction) as $-\beta_r$ and β_f , the COP position u needs to satisfy $x_s - u \leq \beta_r$ and $u - x_s \leq \beta_f$, namely, $-\beta_f \leq u_r \leq \beta_r$, where $\beta_r > 0$ and $\beta_f > 0 (\beta_f + \beta_r = \beta)$ are the distances from m_2 to the rear and front boundaries of BOS, respectively; see Fig. 2(b).

For double-stance phase, two TMLIP models are used for both legs, as shown in Fig. 2(c). We introduce a "virtual" TMLIP model to represent a combined motion of both legs. The virtual TMLIP is created by considering that mass m_1 's

velocity (denoted by \hat{v}) is obtained by $\hat{v} = v_l + v_r$, where v_l and v_r are the velocities that are obtained from the left and right stance's TMLIP, respectively. The virtual mass $\hat{m}_2 = 2m_2$ and its position \hat{x}_s is determined by the intersection point of the normal vector of \hat{v} and the ground; see Fig. 2(c). The BOS is also modified at the new virtual TMLIP support location \hat{x}_s .

B. Slip Recoverability Regions

Given (1) and (2), we rewrite the motion dynamics in a unified form as

$$\ddot{\delta} = \omega^2 \left(\delta + r_m u_r + u_0 \right), \tag{3}$$

where $\omega=\omega_{ns}$ and $u_0=0$ for non-slip gaits, and $\omega=\omega_s$ and $u_0=\mu z_c$ for foot slip gaits. Considering initial conditions $(\delta_0,\dot{\delta}_0)$ and constant input u_r , the solution to (3) is defined by motion manifold, denoted by \mathcal{M} , as a family of hyperbolic curves as

$$\frac{(\delta + r_m u_r + u_0)^2}{(\delta_0 + r_m u_r + u_0)^2 - \frac{\dot{\delta}_0^2}{\omega^2}} - \frac{\dot{\delta}^2 / \omega^2}{(\delta_0 + r_m u_r + u_0)^2 - \frac{\dot{\delta}_0^2}{\omega^2}} = 1.$$
(4)

Motion manifold can be represented geometrically in the δ - δ plane. Fig. 3(a) illustrates the motion manifold \mathcal{M} given by (4) under $u_r = 0$, that is, nominal manifold [10]. The manifolds are considered as in safe region (green-color curves in the figure) if the subject might maintain forward progression without fall, or in fall-prone region (red-color curves) otherwise.

At different locations in the δ - δ plane, two types of fall-prone motions potentially lead to a fall: (i) manifolds leading to backward falls (e.g., \mathcal{M}_1 and \mathcal{M}_2 in Fig. 3(a)); and (ii) manifolds leading to forward falls (e.g., \mathcal{M}_3 and \mathcal{M}_4 in the figure). Using the recoverability concept [10] and considering $-\beta_r \leq u_r \leq \beta_f$, we define safe region \mathcal{R}_s and fall-prone region \mathcal{R}_f in the δ - $\dot{\delta}$ plane as

$$\mathcal{R}_{s} = \{(\delta, \dot{\delta}): \ \dot{\delta} \geq -\omega(\delta + u_{0} + r_{m}\beta_{r}), \text{ and}$$

$$\dot{\delta} \leq -\omega(\delta + u_{0} - r_{m}\beta_{f})\}, \qquad \text{(5a)}$$

$$\mathcal{R}_{f} = \{(\delta, \dot{\delta}): \ \dot{\delta} < -\omega(\delta + u_{0} + r_{m}\beta_{r}), \text{ or}$$

$$\dot{\delta} > -\omega(\delta + u_{0} - r_{m}\beta_{f})\}. \qquad \text{(5b)}$$

The boundaries of \mathcal{R}_s and \mathcal{R}_f are defined as $\partial \mathcal{R}_s^l = \partial \mathcal{R}_f^u = \{(\delta, \dot{\delta}) : \dot{\delta} = -\omega(\delta + u_0 + r_m \beta_r)\}$ and $\partial \mathcal{R}_s^u = \partial \mathcal{R}_f^u = \{(\delta, \dot{\delta}) : \dot{\delta} = -\omega(\delta + u_0 - r_m \beta_f)\}.$

Fig. 3(b) illustrates the safe and fall-prone regions and their boundaries. In this study, we mainly focuses on backward fall, that is, in region \mathcal{R}^b_f in the figure, because it is most commonly happened. Moreover, we use distance to boundary $\partial \mathcal{R}^l_s$ ($\partial \mathcal{R}^u_f$) as a metric to quantify the recovery performance and design target for recovery stepping placement. For example, during slip single-stance phase, the $(\delta,\dot{\delta})$ -trajectory moves from points A to B (further to D) until backward fall as shown in Fig. 3(b). By taking a recovery step, the instantaneous change of δ would bring the state at points B to C (as shown in the figure) in safe region \mathcal{R}_s and therefore, help maintain balance. We will present detailed recovery strategies in Section III.

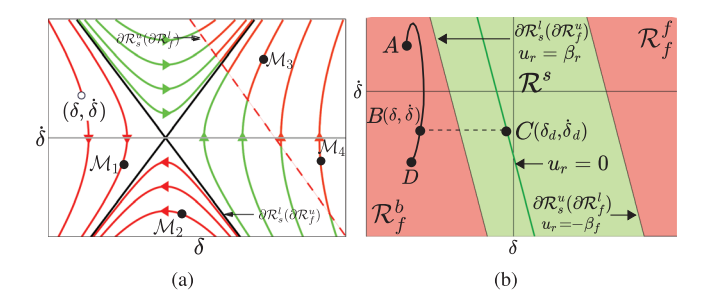


Fig. 3. (a) Nominal manifolds. The green and red curves are considered as safe and fall-prone regions, respectively. (b) Safe region \mathcal{R}_s and fall-prone regions, i.e., \mathcal{R}_f^f for backward falls and \mathcal{R}_f^f for forward falls, with boundaries $\partial \mathcal{R}_s^l$ ($\partial \mathcal{R}_f^u$) and $\partial \mathcal{R}_s^u$ ($\partial \mathcal{R}_f^l$) in the δ - $\dot{\delta}$ plane.

We extend the approach in [18] for real-time slip detection using the wearable IMUs. A slip indicator, denoted as $S_I(t)$, is used to detect the foot slip onset time in real time. The slip indicator uses both measured angular and linear accelerations from the IMUs to ensure higher detection accuracy and lower latency. An extended Kalman filter (EKF) is also used and implemented to estimate the stance foot slipping velocity v_s in real time. For details about the slip detection algorithm and EKF design, readers can refer to [18].

III. EXOSKELETON CONTROL DESIGN

In this section, we first analyze human-inspired gait recovery strategies and then present the exoskeleton controller.

A. Human-Inspired Recovery Analysis

Studying how humans recover from unexpected foot slip can provide insights into designing exoskeleton controllers, therefore we conducted human subject experiments and collected data of successful recovery gaits under unexpected foot slip [18]. Fig. 4 shows the left- and right-knee joint angles and moments during normal walking and slip-induced-fall recovery. Normal walking gait consists of single- and double-stance phases and similarly slip single- and double-stance phases for gaits under foot slip. The slip-recovery gait (dashed lines) is normalized with respect to a normal walking stride duration (solid lines). The slip started after the right-foot heel touchdown and the left-foot toeoff. For the swing leg, a large increase in the knee extension direction was observed as the slip started because the subject tried to land the swing leg as quickly as possible to maintain balance. This was also observed from a large increase of knee moment (left-bottom plot in the figure). For the slipping stance leg, the knee moment increased in the flexion direction as the subject tried to slow down the slipping velocity. Finally, the gait recovered successfully and both knee joints provided extension moments to avoid limb-collapse fall.

The above observation confirms that higher knee extension strength, such as greater knee peak torque and greater rate of torque development, is critical for slip balance recovery [3]. The reactive knee joint moment of the slipping stance leg tends to slow down the sliding motion to reduce the slip severity and prevent body falling, which was also reported in [22]. The swing

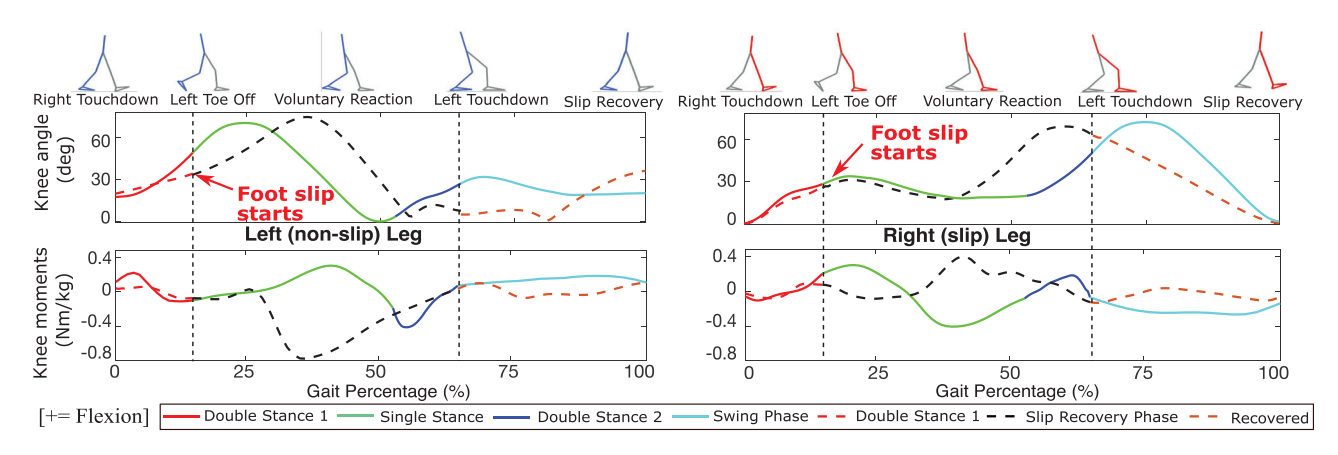


Fig. 4. Human knee angles and moments during normal walking gait and successful recovery gait of backward slip-induced falls. The left and right columns are for left (non-slip) and right (slip) legs, respectively. The solid and dashed lines are for normal and slip walking gaits, respectively. The top snapshots (with vertical dashed lines) indicate the major walking gait events during slip recovery gait. The slip walking gait starts at the right foot touchdown and the plot is normalized with respect to normal walking gait duration.

leg's large extension knee moment is responsible for moving towards the CP and land the swing foot onto the ground. These observation and evidences are used for the exoskeleton control in Section III-C.

B. Exoskeleton Control Overview

Fig. 5 illustrates the flowchart of the slip detection and exoskeleton control design. The IMU-based slip detection system begins at the heel strike moment, and determines the onset of the foot slip and slipping velocity estimation. If the slip indicator $S_I \geq S_{\rm thd}$, where $S_{\rm thd}$ is the indicator threshold, a foot slip event is declared and the slipping velocity v_s is estimated from the EKF in real time. The gait recovery controller is designed to help subject place the swing leg at the desired location and meanwhile decrease the slipping velocity of the stance leg. When the swing leg touches down on the ground or the slipping velocity is less than a threshold value ϵ_v , the anti-collapse controller is applied to both legs. When the difference between the knee angles and their equilibria is within a threshold ϵ_q , the subject is considered as stable stance. In the following, we describe the exoskeleton control for normal walking and balance recovery under foot slip.

For normal walking gait, we take the stiffness-based continuous assistive controller from [23]. The stiffness-based design also serves as a baseline controller for comparison purpose. The applied assistive torque by the exoskeleton at each leg is

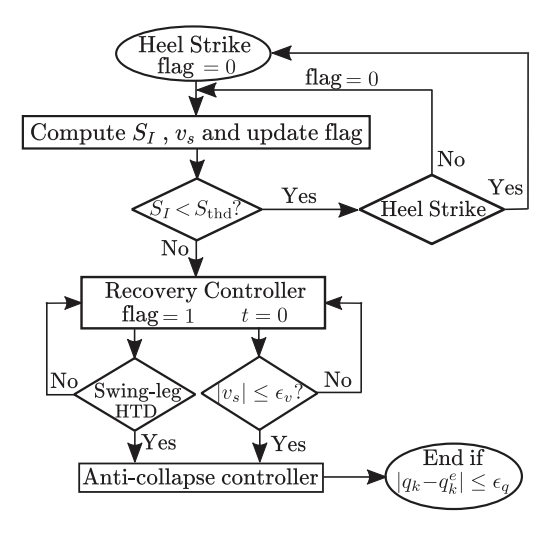


Fig. 5. Flowchart of the overall exoskeleton controller design.

C. Gait Recovery Controller

When slip initiates at heel touchdown and left-foot toeoff, the COM lags behind the COP and the body tends to fall backward. The exoskeleton control is to provide assistive torques for both legs to adjust the COP position.

1) Swing Leg Foot-Placement Controller: During slip single-stance phase, the trailing leg swings off the ground. Inspired by successful human recovery gait, the control strategy is to land the swing leg on the ground as quickly as possible and to reset the ZMP to avoid a fall. We need two critical designs: one is the targeted foot touchdown location and the other is motion profile for the swing leg.

To design the touchdown location for the swing leg, we use the safe and fall-prone regions given in (5). When slip starts, the $(\delta, \dot{\delta})$ -trajectory is about to deviate from safe region \mathcal{R}_s to fall-prone region \mathcal{R}_f ; see Fig. 3(b). For any state (e.g., point $B(\delta, \dot{\delta})$) in \mathcal{R}_f , the goal of the recovery step is to bring back to a desired state (e.g., point $C(\delta_d, \dot{\delta}_d)$) in \mathcal{R}_s . The desired state is located on the asymptote $\dot{\delta} = \dot{\delta}_d = -\omega_s(\delta_d + \mu z_c)$ (i.e., setting

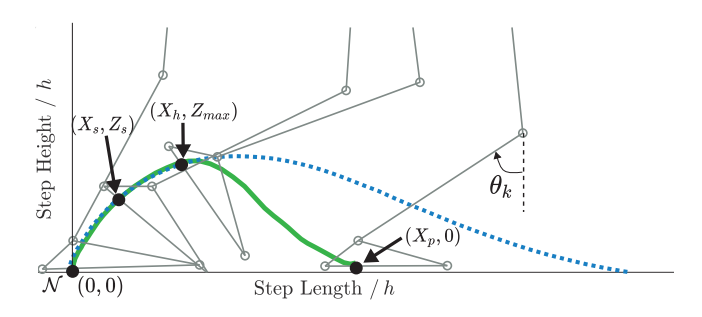


Fig. 6. Swing leg trajectory planning with the normalized (X, Z). The dotted blue line is for normal walking and solid green line for slip recovery.

 $u_r=0$ in (4)). Denoting the desired foot placement as x_p , then $\delta_d=x_p-x_1$ and we obtain

$$x_p = x_s - (\delta_d - \delta) = x_s + \mu z_c + \frac{\dot{\delta}}{\omega_s} + \delta.$$
 (7)

To design the swing leg controller that complies with subjects' motion, multiple experiments were conducted and the swing foot trajectories of recovery gaits were collected. To obtain the swing foot trajectory (x, z), we use the normalized variables X = x/hand Z = z/h, where h is the human height. By normalizing the trajectories, the experimental data indicates that a third-order polynomial can smoothly capture swing foot trajectories in the (X-Z) plane, as shown in Fig. 6. The origin of frame \mathcal{N} is considered at the foot touchdown location. Denoting the current location of the swing foot as (X_s, Z_s) and with the targeted foot placement location $X_p = x_p/h$ from (7) (i.e., $(X_p, 0)$), a third-order polynomial is built to generate the swing foot trajectory from (X_s, Z_s) to $(X_p, 0)$. Due to the momentum of moving gaits, the swing foot always passes through a point at $(X_p/2, Z_{\text{max}})$, where Z_{max} is a specified height. This point is used to determine the polynomial coefficients.

With the planned swing leg trajectory, we use the two-link lower-limb kinematics to compute desired knee joint angle profile, denoted as θ_k^d . An impedance exoskeleton torque controller is used to expedite the touchdown motion and to land the swing foot close to the desired position, namely,

$$\tau_{k,sw} = k_T \left(\theta_k - \theta_k^d \right) + b_T \left(\dot{\theta}_k - \dot{\theta}_k^d \right), \tag{8}$$

where k_T and b_T are proportional and derivative gains, respectively, and $\dot{\theta}_k^d$ is obtained by numerical differentiation.

2) Slipping Stance-Leg Controller: From successful human recovery gait, the applied flexion torques to the stance leg help decrease the slipping velocity and further save the lower-limb to collapse. Therefore, we design the exoskeleton controller to provide counter-slip torque for the slipping stance leg as

$$\tau_{k,st} = k_s \hat{v}_s,\tag{9}$$

where k_s is the propotional gain and \hat{v}_s is the EKF-based estimate of slipping velocity v_s .

3) Anti-Collapse Controller: As we observed in experiments, human subjects tended to flex the support leg, which decreased the slip velocity but also caused that the knee flexion angle of the slipping stance leg increased continuously. Therefore, after the slipping velocity decreases below a threshold value ϵ_v , the exoskeleton needs to exert assistive torques to

avoid limb-collapse-induced fall. We design a stiffness-based anti-collapse controller as

$$\tau_{k,ac} = k_{AC} m_h \left(\theta_k - \theta_k^e \right), \tag{10}$$

where k_{AC} is stiffness constant and θ_k^e is equilibrium knee joint angle at stance. In implementation, we estimated the knee joint stiffness with knee angle and moment profiles that were reported in [20].

IV. EXPERIMENTS

A. Experimental Setup and Protocols

Fig. 7(a) shows the wearable sensors, bilateral exoskeletons and integrated embedded and computing devices. Seven IMUs (from LP-RESEARCH Inc.) were attached to the the subject's pelvis, left- and right-thighs, shanks, and heels for data collection and exoskeleton control, as shown in Fig. 2(a). Each individual IMU includes a 3-axial magnetometer, gyroscope and accelerometer. A set of 16 reflective markers were attached to human subjects and a motion capture system (9 Vantage cameras from Vicon Ltd.) was used to obtain the lower limbs joint angles. Motion data from the wearable IMUs and motion capture system were collected at a 100-Hz frequency.

The knee exoskeleton design is compact and light-weight (unilateral unit weighed 1.7 kg), and provides high-torque output (35 Nm peak torque), large range of motion (0–160 deg flexion), and high rotation speed (16.2 rad/s). The low-level controller conducts torque control through the controller area network (CAN) protocol at 300 Hz. It also communicates with the high-level control device (Linux embedded system) through a serial-port interface. The high-level torque controller runs at 100 Hz and takes the joint angles (from IMUs) as inputs. The exoskeleton is powered by a 36 V Lithium battery with running time up to 2 hours.

Six young subjects (two female and four male; age: 24.7 ± 3.3 years; height: 170 ± 5 cm; weight: 74.1 ± 11.1 kg) were recruited to participate in experiments. All participants self-reported to be able bodied and in a good health condition. An informed consent form was signed by all subjects and the testing protocol was approved by the Institutional Review Board (IRB) at Rutgers University. Fig. 7(b) shows the indoor laboratory setup for unexpected slip experiments. Foot slip was reliably initiated on the soap water-contaminated floor. The shoe/floor friction coefficient was measured and confirmed around $\mu = 0.1$ [24].

The subjects were instructed to wear a pair of half-covered goggles, and walk straight on a 7-meter path at their preferred speed. The subjects were required to walk back and forth for 5 times to get familiar with the devices. They were informed that there might or might not be a slip during the trial, and therefore, a foot slip was unpredictable. To ensure their safety, a body safety harness was used with a rope length that did not hinder their movements but protected them from falls. The subjects were asked to step out the right foot at the starting point so that they stepped on the same region every time. The soap water was precisely applied to the heel strike position and leading to slip in walking direction only, allowing for slip initiation

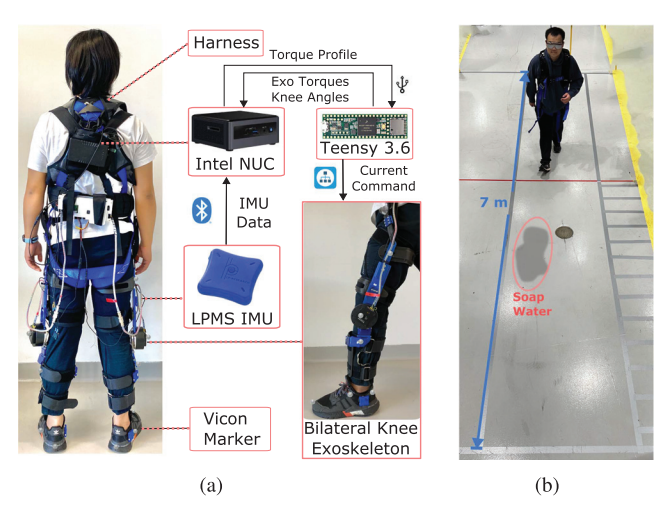


Fig. 7. (a) Wearable sensing units, exoskeletons with integrated embedded and computing systems and the interconnection among them. (b) Indoor laboratory setup for slip detection and gait recovery experiments.

while minimizing any potential joint harm to participants. A slip-induced fall was declared if the hip height decreased over 15 % of its minimum value of normal walking.

Each subject was asked to run three groups of experiments for multiple times: Group A: no exoskeleton; Group B: exoskeleton with the baseline controller (6); and Group C: exoskeleton with the recovery controller (8)–(10). To make sure that the subjects performed same reactions, they were asked to conduct these three groups of experiment once the other day. Control systems parameters were implemented as follows: $k_{st}=0.038,\,k_{sw}=0.0046,\,\theta_{sw}^e=57.52$ deg, $\theta_{st}^e=5.33$ deg, $k_T=10,\,b_T=0.05,\,k_{AC}=5,\,k_s=5,\,S_{\rm thd}=1.57,\,\gamma=-377$ deg/s, $\epsilon_v=0.2$ m/s, and $\epsilon_q=5$ deg.

B. Experimental Results

The experimental data was collected from 16 trials in each group. In Group A, 10 trials were unsuccessful in recovering without the exoskeleton. In Group B, 5 trials were unsuccessful in recovering with the exoskeleton and baseline controller. In Group C, all trials successfully recovered from unexpected foot slips with the proposed exoskeleton controller. During normal walking without foot slip, subjects had similar kinematic motions (hip, knee, and ankle angles) regardless of exoskeleton use (i.e., p > 0.99), and therefore the use of the exoskeletons was considered transparent.

Fig. 8 shows the kinematic data and the exoskeleton output from Subject S4 from the time moment of slip occurrence (as t=0) to 400 ms after that. A normal walking gait was also plotted for comparison. Subject S4 fell without wearing the exoskeletons, and recovered with the exoskeletons under both the baseline and recovery controllers. Under unexpected slip, the lower-limb kinematic motions showed a significant change. In particular, the hip and knee joints of the stance leg showed more extended compared to the normal walking gait. Compared with the baseline controller, the recovery control demonstrates

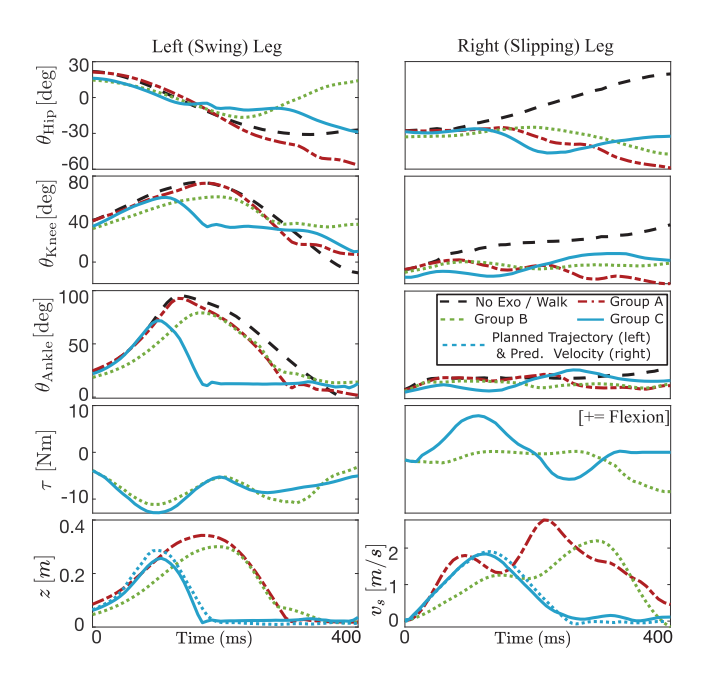


Fig. 8. Joint angles (thigh, knee and ankle), exoskeleton torques at the swing leg (left column) and slipping leg (right column) for four experimental conditions: normal walking without exoskeleton (black lines); Group A (red lines); Group B (green lines); and Group C (blue lines). The last row indicates the swing foot trajectory and slipping velocity, respectively.

different performance. Under the baseline controller, an extension torque was applied on the swing leg, and the stance leg also experienced a small extension torque, which did not result in a slipping velocity decrease. In contrast, the recovery controller was initiated at $t=35\,\mathrm{ms}$ when slip was detected. The swing-leg trajectory touched down much faster ($t=180\,\mathrm{ms}$) than that under the baseline control ($t=300\,\mathrm{ms}$). Moreover, the applied torque greatly decreased the slipping velocity and the stance leg stopped shortly after touchdown ($t=270\,\mathrm{ms}$). Finally, the anti-collapse controller prevented subjects falling from insufficient support with consistent extension torques. The online planned swing leg trajectory shown at the bottom-left plot fitted well with the real touchdown trajectory. The EKF-based slipping velocity estimates matched the actual values closely.

Fig. 9(a) shows the slip detection latency and slipping velocity estimates of each subject (mean and standard deviation). The ground truth of the slip occurrence was determined by the captured motion data and the detection latency was computed as the difference between the IMU-based detection time and the ground-truth slip onset time. The slip detection system identified all slips within 110 ms after their occurrence with slipping velocity up to 1.2 m/s. The average slip detection latency of all experiments is 63.2 ± 22.3 ms. The safe margin stability is calculated as the minimum distance from the $(\delta, \dot{\delta})$ -trajectory to $\partial \mathcal{R}_s^l$ in the δ - $\dot{\delta}$ plane (positive when in \mathcal{R}_s and negative in \mathcal{R}_f ; see Fig. 3(b)). Fig. 9(b) compares the safe margin stability among the three groups. The safe margin stability significantly improved with the recovery controller compared with the baseline controller or without exoskeleton.

Fig. 9(c) compares the swing leg's ROM, step height, and touchdown time for all trials during foot slip. With the recovery

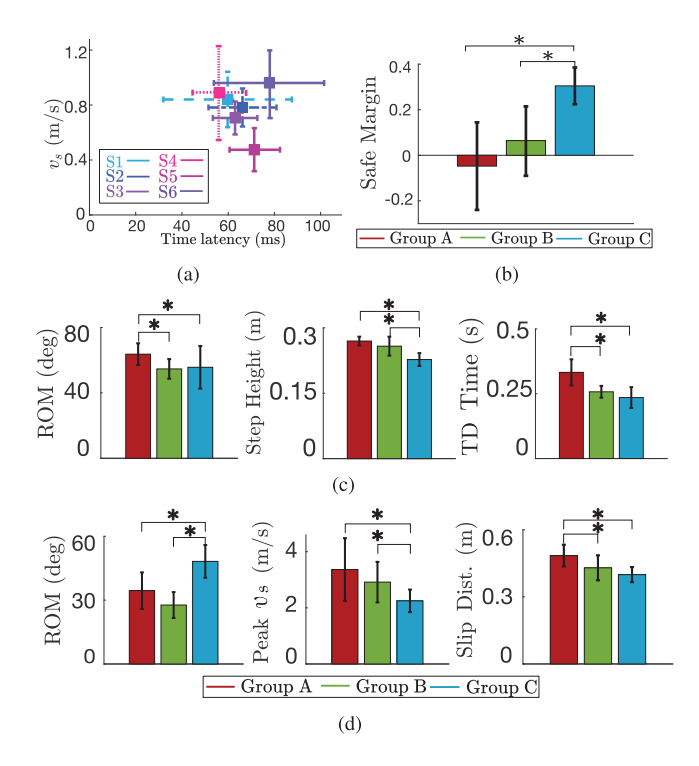


Fig. 9. (a) Comparison of the slip velocity v_s and the slip detection latency (mean value and standard deviation) for each subject. (b) The safe margin stability comparison (mean value and standard deviation) among Groups A, B, and C. (c) ROM, step height, and touchdown time comparison (mean value and standard deviation) of the swing leg among Groups A, B, and C. (d) ROM, peak slipping velocity, and slipping distance comparison (mean value and standard deviation) of the slipping leg among Groups A, B, and C. The label * indicates a significant (p < 0.05) difference among trials.

TABLE I
KINEMATIC DATA COMPARISON BETWEEN THREE GROUPS

Group	x_s (m)	$v_s^{max}(m/s)$	Stability	TD Time (ms)
A	0.48 ± 0.05	3.2 ± 1.12	-0.05 ± 0.19	332 ± 50
В	0.43 ± 0.06	2.9 ± 0.72	0.06 ± 0.15	258 ± 23
С	0.39 ± 0.03	2.1 ± 0.40	0.30 ± 0.08	235 ± 40

controller, the swing leg's ROM showed greater variation due to extension torques. Both the baseline and recovery controllers reduced step heights with smaller variance, which increased the chance of successful recovery. The recovery controller further reduced step heights with the planned trajectory. Additionally, the average touchdown time of Group C was significantly reduced compared to Groups B and C. Similarly, Fig. 9(d) shows that the ROM of the slipping leg significantly increased under the recovery controller, indicating flexion motion and balance recovery. Furthermore, the peak slipping velocity was notably reduced by the applied flexion torques on the stance leg. This trend was also observed for slipping distance, and the recovery controller was found to be the most effective.

Table I summarizes the numeric values of the selected metrics. From the results in the table, the touchdown time of the subjects in Group C was obviously decreased by about $90 \, \mathrm{ms}$ compared with Group A and about $23 \, \mathrm{ms}$ compared with Group B. Same trend is also observed for maximum slipping velocity, the slip

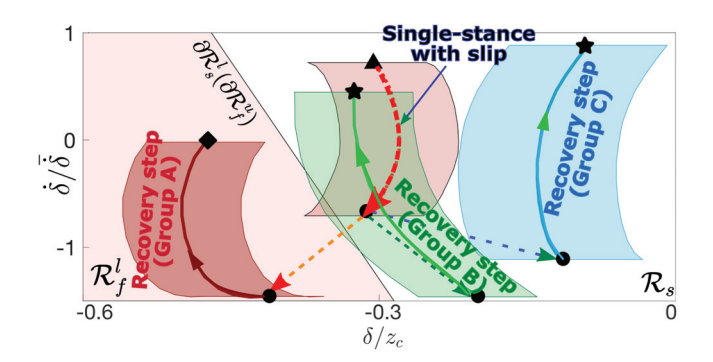


Fig. 10. Recovery motion manifold comparison among three groups. The red shaded area (mean and standard deviation) represents the unsuccessful recovery cases in Group A and B, while the green and blue shaded areas (mean and standard deviation) represent the successful recovery cases in Groups B and C, respectively. The triangle markers " \blacktriangle " represent the onset of the slip, circular markers " \bullet " represent the beginning of recovery steps, the stars markers " \bigstar " represent the ending points of successful recovery gaits (Groups B and C) and the diamond marker " \blacklozenge " represent the ending point of unsuccessful recovery gait (Group A).

distance, and the safe margin stability. A one-way repeated measures analysis of variance (ANOVA) was conducted to evaluate the impacts of the exoskeleton on the above-mentioned metrics. The *p*-values for all seven metrics were significantly less than 5%. A Tukey test was performed and it demonstrated that the exoskeletons provided assistive torques to enhance balance recovery under unexpected foot slip for different subjects with no need of training, (see Fig. 9(b), (c), and (d)).

Fig. 10 further shows the recovery trajectory profiles in the δ - δ plane for 18 experiment trials (one representative trial from each subject under each group). The (δ, δ) -trajectory started in fall-prone region \mathcal{R}_f in single-stance phase (red thick dashed line as the mean value and the pink shared area as the standard deviation) with foot slip. When the swing-leg touched down, the trajectories split into three different groups. The red shaded area (mean and standard deviation) shows the unsuccessful recovery (Group A and part of Group B). The subjects tried to maintain balance but because of either slow response or improper foot placement, the COP were not reset into the BOS and no recovery was obtained. The green shaded area (mean and standard deviation) is the successful recovery under the baseline control (Group B). Although the controller brought the gaits into the safe region, the (δ, δ) -trajectory was close to the safety boundary with small recoverable margins. Finally, under the recovery control (i.e., blue shaded area from Group C), the swing leg touched down in the safe region with exoskeleton assistance, and the trajectory calculated from the TMLIP model was maintained far away from the safety boundary.

C. Discussion

The main contribution of this work is the integrated wearable sensing and knee exoskeleton system for balance recovery control under unexpected foot slip. This work presents a systematic analysis and design of knee exoskeleton-enabled gait recovery under slip perturbation. The selection of the knee exoskeleton for this investigation is well-justified, given its documented significance in slip recovery gait [22]. All the presented results

indicate that the intergrated knee exoskeleton system provided assistive toruqes to promote balance recovery under foot slip. The exoskeleton control was also adaptable to different subjects without requiring any trainning for successful implementation. The averaged detection time of the IMU-based slip detection system was around 63 ms, which is much shorter than human voluntary reaction time (around 200 ms [25]) and joint angle based detection method [17] (about 350 ms). Unlike the simulated foot slip perturbation on treadmill (e.g., [17]), this work used real-life slip generation experiments and therefore, reflects slip recovery reality.

Although this work primarily focuses on backward falls (i.e., \mathcal{M}_1 and \mathcal{M}_2 in Fig. 3(b)), the recovery control strategy can be further extended to handle other types of falls, such as the manifolds leading to forward falls (i.e., \mathcal{M}_3 and \mathcal{M}_4 in Fig. 3(b)). Moreover, the motion manifold in Fig. 3 is related to the margin of stability (MOS) that was presented in [17], [26]. The MOS was built on single-mass LIP model with the assumption that $x_s = \dot{x}_s = 0$, which cannot capture ankle-actuated moments under slip condition. We therefore proposed to use the relative position δ of the TMLIP model to address the shortcoming of the LIP model. The use of the safe and fall-prone regions not only enables to determine the recoverability condition but also helps design the desired targeted COP profile.

There are still some limitations in this study. For example, the slip detection system needs to use seven wearable IMUs and the communication between the IMUs, upper-level controller, and the exoskeleton is redundant. Furthermore, the control strategies are based on the TMLIP in the anterior-posterior plane. One recent research work indicated that humans reacted to unexpected slips in both lateral and anterior-posterior directions [27]. It would be helpful to extend the research to consider motions in the lateral direction. It is also desired to further reduce the device weight for personal daily activities.

V. CONCLUSION

This letter presented a thorough analysis of biomechanics, slip dynamics, and exoskeleton control strategy for balance recovery in human walking gait under unexpected foot slip. The TMLIP model and motion manifolds were extended to investigate gait recoverability under foot slip perturbation, and foot-placement and gait recovery strategies were presented for knee exoskeleton control to maintain gait balance. Experimental results demonstrated the effectiveness of the exoskeleton controller in enhancing gait recovery and confirmed its superiority over the baseline walking assistive control. One future research direction includes improving wearable sensing and exoskeleton systems to prevent potential slip-and-fall incidents for industrial workers in workspace.

REFERENCES

- S. Heinrich, K. Rapp, U. Rissmann, C. Becker, and H.-H. König, "Cost of falls in old age: A systematic review," *Osteop. Int.*, vol. 21, no. 6, pp. 891–902, 2010.
- [2] M. S. Redfern et al., "Biomechanics of slips," *Ergonomics*, vol. 44, no. 13, pp. 1138–1166, 2001.

- [3] S. A. Wyszomierski, A. J. Chambers, and R. Cham, "Knee strength capabilities and slip severity," *J. App. Biomech*, vol. 25, pp. 140–148, 2009.
- [4] A. J. Young and D. P. Ferris, "State of the art and future directions for lower limb robotic exoskeletons," *IEEE Trans. Neural Syst. Rehab. Eng.*, vol. 25, no. 2, pp. 171–182, Feb. 2017.
- [5] G. S. Sawicki, O. N. Beck, I. Kang, and A. J. Young, "The exoskeleton expansion: Improving walking and running economy," *J. Neuroeng. Rehabil.*, vol. 17, 2020, Art. no. 25.
- [6] S. Chen et al., "Wearable knee assistive devices for kneeling tasks in construction," *IEEE/ASME Trans. Mechatron.*, vol. 26, no. 4, pp. 1989–1996, Apr. 2021.
- [7] Y. Ma, X. Wu, J. Yi, C. Wang, and C. Chen, "A review on human-exoskeleton coordination towards lower limb robotic exoskeleton systems," *Int. J. Robot. Automat.*, vol. 34, no. 4, pp. 431–451, 2019.
- [8] L. Zhang, G. Liu, B. Han, Z. Wang, H. Li, and Y. Jiao, "Assistive devices of human knee joint: A review," *Robot. Auton. Syst.*, vol. 125, 2020, Art. no. 103394.
- [9] J. Pratt, J. Carff, S. Drakunov, and A. Goswami, "Capture point: A step toward humanoid push recovery," in *Proc. IEEE Int. Conf. Humanoid Robots*, 2006, pp. 200–207.
- [10] M. Mihalec, M. Trkov, and J. Yi, "Balance recoverability and control of bipedal walkers with foot slip," ASME J. Biomech. Eng., vol. 144, no. 5, 2022, Art. no. 051012.
- [11] M. Mihalec, F. Han, and J. Yi, "Integrated inverted pendulum and whole-body control design for bipedal robot with foot slip," *IFAC PapersOnLine*, vol. 55, no. 37, pp. 376–381, 2022.
- [12] M. Mihalec and J. Yi, "Balance gait controller for a bipedal robotic walker with foot slip," *IEEE/ASME Trans. Mechatron.*, vol. 28, no. 4, pp. 2012–2019, Apr. 2023.
- [13] W.-L. Ma, Y. Or, and A. D. Ames, "Dynamic walking on slippery surfaces: Demonstrating stable bipedal gaits with planned ground slippage," in *Proc. IEEE Int. Conf. Robot. Autom.*, 2019, pp. 3705–3711.
- [14] T. Chen and B. Goodwine, "Robust gait design for a compass gait biped on slippery surfaces," *Robot. Auton. Syst.*, vol. 140, 2021, Art. no. 103762.
- [15] A. Agrawal et al., "First steps towards translating hzd control of bipedal robots to decentralized control of exoskeletons," *IEEE Access*, vol. 5, pp. 9919–9934, 2017.
- [16] M. Mioskowska, D. Stevenson, M. Onu, and M. Trkov, "Compressed gas actuated knee assistive exoskeleton for slip-induced fall prevention during human walking," in *Proc. IEEE/ASME Int. Conf. Adv. Int. Mechatron.*, 2020, pp. 735–740.
- [17] V. Monaco et al., "An ecologically-controlled exoskeleton can improve balance recovery after slippage," Sci. Rep., vol. 7, 2017, Art. no. 46721.
- [18] M. Trkov, K. Chen, J. Yi, and T. Liu, "Inertial sensor-based slip detection in human walking," *IEEE Trans. Automat. Sci. Eng.*, vol. 16, no. 3, pp. 1399–1411, 2019.
- [19] S. Yu et al., "Quasi-direct drive actuation for a lightweight hip exoskeleton with high backdrivability and high bandwidth," *IEEE/ASME Trans. Mechatron.*, vol. 25, no. 4, pp. 1794–1802, Aug. 2020.
- [20] S. Wang, T. Bhatt, X. Liu, and Y.-C. Pai, "The role of recovery lower limb segments in post-slip determination of falls due to instability or limb collapse," *Ann. Biomed. Eng.*, vol. 48, no. 1, pp. 192–202, 2020.
- [21] K. Chen, M. Trkov, S. Chen, J. Yi, and T. Liu, "Balance recovery control of human walking with foot slip," in *Proc. IEEE Amer. Control Conf.*, 2016, pp. 4385–4390.
- [22] B. Moyer, M. Redfern, and R. Cham, "Biomechanics of trailing leg response to slipping-evidence of interlimb and intralimb coordination," *Gait Posture*, vol. 29, no. 4, pp. 565–570, 2009.
- [23] T. H. Huang et al., "Modeling and stiffness-based continuous torque control of lightweightquasi-direct-drive knee exoskeletons for versatile walking assistance," *IEEE Trans. Robot.*, vol. 38, no. 3, pp. 1442–1459, Mar. 2022.
- [24] M. Trkov, J. Yi, T. Liu, and K. Li, "Shoe-floor interactions human walking with slips: Modeling and experiments," ASME J. Biomech. Eng., vol. 140, no. 3, 2018, Art. no. 031005.
- [25] D. S. Marigold and A. E. Patla, "Strategies for dynamic stability during locomotion on a slippery surface: Effects of prior experience and knowledge," *J. Neurophysiol.*, vol. 88, pp. 339–353, 2002.
- [26] A. L. Hof, "The 'extrapolated center of mass' concept suggests a simple control of balance in walking," *Hum. Movement Sci.*, vol. 27, pp. 112–125, 2008.
- [27] C. M. Rasmussen and N. H. Hunt, "Unconstrained slip mechanics and stepping reactions depend on slip onset timing," *J. Biomech.*, vol. 125, 2021, Art. no. 110572.